MOF-derived ZnO and ZnO@C composites with high photocatalytic activity and adsorption capacity

Seung Jae Yang, Ji Hyuk Im, Taehoon Kim, Kunsil Lee, Chong Rae Park*

Carbon Nanomaterials Design Laboratory, Global Research Laboratory, Research Institute of Advanced Materials, and Department of Materials Science and Engineering, Seoul National University, Seoul 151-744, South Korea

ABSTRACT

Nanostructured ZnO materials have unique and highly attractive properties and have inspired interest in their research and development. This paper presents a facile method for the preparation of novel ZnO-based nanostructured architectures using a metal organic framework (MOF) as a precursor. In this approach, ZnO nanoparticles and ZnO@C hybrid composites were produced under several heating and atmospheric (air or nitrogen) conditions. The resultant ZnO nanoparticles formed hierarchical aggregates with a three-dimensional cubic morphology, whereas ZnO@C hybrid composites consisted of faceted ZnO crystals embedded within a highly porous carbonaceous species, as determined by several characterization methods. The newly synthesized nanomaterials showed relatively high photocatalytic decomposition activity and significantly enhanced adsorption capacities for organic pollutants.

© 2010 Elsevier B.V. All rights reserved.

1. Introduction

Metal organic frameworks (MOFs) are a rapidly growing class of adsorbent material with the remarkable characteristics of well-defined channels and cavities of regular size and shape that are easily tunable on the nanometer scale [1–3]. These fascinating properties of MOFs make them ideal candidates for the storage of gas molecules, for example, hydrogen, or the entrapment of large amounts of greenhouse gases [4–6]. A unique aspect of MOFs that form highly flexible frameworks that undergo structural and mechanical changes in response to specific stimuli have inspired a variety of other potential applications, including gas separation, catalysis, chiral separation, sensing, and gas chromatography [7,8]. Strategies for utilizing MOFs have focused on maximizing their porous characteristics.

In the past few years, several studies of the semiconducting properties of MOFs have been reported. Seifert et al. suggested in a theoretical work that MOFs are semiconductors with band gaps between 1.0 and 5.5 eV [9]. In contrast, Bordiga et al. and Alvaro et al. reported that MOFs behave as metal oxide quantum dots [10]. Garcia et al. showed that MOF-5 nanoparticles behave as microporous semiconductors with a wide band gap upon excitation with UV light, and they undergo charge separation, after which the excited delocalized electrons remain stable on the microsecond time scale [11]. Nevertheless, applications of MOFs to semiconductor research remains unexplored, probably due to the instability of

MOFs with respect to thermal treatments, moisture, or chemical agents [6,12].

We demonstrate herein that ZnO nanoparticles and ZnO@C composites may be easily prepared via simple heat treatments of MOF-5 under a variety of atmospheric gaseous conditions. Hierarchical aggregates of ZnO nanoparticles formed during heat treatment under an air atmosphere, and ZnO@C composites with high specific surface areas (SSA) (>500 m^2/g) were produced under a nitrogen atmosphere. Interestingly, the MOF-derived ZnO nanoparticles exhibited high photocatalytic degradation of Rhodamine-B (RhB) under ultraviolet (UV) irradiation comparable to degradation by P25 (commercial TiO$_2$) [13]. The ZnO@C composites showed a much higher adsorption capacity for RhB than did ST01 (commercial TiO$_2$), despite comparable SSA values. MOF-derived ZnO and ZnO@C composites may potentially be used to remedy organic pollution in water and air environments.

2. Experimental

2.1. Reagents and chemicals

Zinc nitrate tetrahydrate (Merck), terephthalic acid (Aldrich), N,N'-dimethylformamide (DMF; Daejung, Korea), RhB (Aldrich), P25 (Degussa Co., Germany), and ST-01 (Ishihara, Japan) were used without further purification or modification.

2.2. Characterization

Field-emission scanning electron microscopy (FE-SEM; JSM6330F, JEOL), transmission electron microscopy (TEM; Tecnai

* Corresponding author. Tel.: +82 2 880 8030; fax: +82 2 885 1748.
E-mail address: crpark@snu.ac.kr (C.R. Park).

F20, FEI), equipped with electron energy loss spectroscopy (EELS), and energy dispersive spectroscopy (EDS) were used to identify the morphological structure, chemical composition, and chemical bonding status within the products. Powder X-ray diffraction (PXRD) was carried out on a D8 Advance (Bruker) diffractometer according to standard procedures [14]. The diffractograms were recorded in reflection mode using Ni-filtered CuKα radiation (λ = 0.154184 nm). The powdered samples were scanned from 5° to 90° using a step size of 0.02° and a run time of 1 s/step at operation condition of 40 kV and 40 mA. Nitrogen adsorption isotherms at liquid nitrogen temperature (77 K) were measured with a Micromeritics ASAP 2020 static volumetric gas adsorption instrument. All gas sorption isotherms were obtained using ultra-high purity grade (99.999%) gas. Prior to gas sorption analysis, the samples (0.1–0.2 g) in the chamber were placed under a vacuum of 10^{-5} Torr with heating at 200 °C for 6 h. The absorptivity and photocatalytic activity were examined using a UV-visible absorption spectrometer (Cary 5000, Varian). Photoluminescence (PL) was examined on a PL spectroscopy (Shimadzu RF-5301 PC).

2.3. Preparation of MOF-5 crystals

Zinc nitrate tetrahydrate (0.7840 g, 3 mmol) and terephthalic acid (0.166 g, 1 mmol) were dissolved in 30 mL DMF in a vial. The reaction mixture was heated in an oven at 105 °C for 24 h to yield cubic crystals of MOF-5. The reaction vessel was then removed from the oven and allowed to cool to room temperature. The obtained cubic crystals were repeatedly washed with DMF and anhydrous chloroform and soaked in anhydrous chloroform for 24 h, followed by filtration.

2.4. Preparation of ZnO nanoparticles and ZnO@C hybrid composites

The prepared MOF-5 was transferred into a tube furnace and heat-treated at 600–700 °C under air with a heating rate of 5 °C/min to pyrolyze the organic species. After reaching the target temperature, the material was allowed to cool to room temperature. The final products (ZnO nanoparticles) revealed a white-colored cubic morphology. The samples were designated xxxA or xxxA_3h, where xxx, A, and 3h denote the heating temperature, the heating atmospheric conditions (air), and heating time at the target temperature, respectively. The ZnO@C composites were prepared by the same method as those used in the case of ZnO nanoparticles, except for the atmospheric conditions. In this case, an inert nitrogen gas was used to obtain black-colored cubic ZnO@C composites. The samples were designated 600N or 600N_3h, where 600, N, and 3h denote the heating temperature, heating atmospheric conditions (nitrogen), and heating time at the target temperature, respectively.

2.5. Adsorption and photocatalytic decomposition of RhB

A RhB solution with a concentration of 24 mg/L (5×10^{-5} M) was prepared by dissolving the dye in distilled water. Twenty-five milligrams of the sample was then dispersed into the RhB solution (20 mL). The resultant mixture was stirred in the dark for a fixed time to evaluate the adsorption capacity. The concentration of RhB was analyzed using a UV-vis spectrometer, and the time-dependent absorption at 554 nm was recorded.

The photocatalytic decomposition of RhB was studied using the prepared RhB stock solution. After stirring in the dark for a fixed time to reach adsorption–desorption equilibrium, the resultant mixture was exposed to UV irradiation (20 W, Shimadzu) under stirring. The decomposition of RhB was followed by measuring the absorbance of the solution at 554 nm as a function of irradiation time, and the remaining sample was removed by syringe filtration.
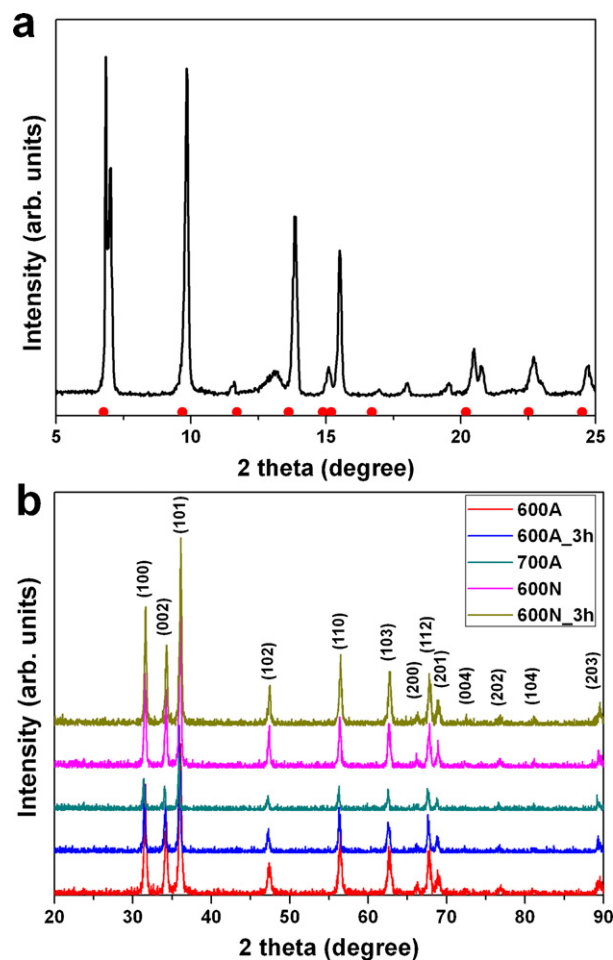

Fig. 1. (a) PXRD pattern for the synthesized MOF-5 and simulation of ideal MOF-5. Peak positions are indicated by solid dots below the PXRD pattern. (b) PXRD patterns of the products prepared under various synthetic conditions.

3. Results and discussion

3.1. Structural and morphological characteristics of ZnO nanoparticles and ZnO@C composites

The MOF-5 derivatives presented different colors, depending on the atmospheric conditions. Thermal treatment of MOF-5 under air resulted in a white product, whereas a black product was obtained under nitrogen, indicating the presence of carbonaceous species.

PXRD patterns of all products showed the changes in the phase structure of MOF-5 to ZnO, as shown in Fig. 1. The obtained MOF-5 exhibited peak positions that were similar with the theoretically predicted XRD patterns of MOF-5 (Fig. 1a) and the reported experimental values for MOF-5s [15,16]. Differences in the relative peak intensities were ascribed to the doubly interwoven frameworks obtained from typical DMF-based synthesis [2]. All MOF-5 derivatives gave PXRD patterns with sharp reflections (Fig. 1b) attributed to crystalline ZnO with a hexagonal wurtzite structure, independent of heating conditions [17–20]. The carbonaceous species of the black ZnO@C (600N and 600N_3h) were confirmed to be amorphous phases due to the absence of a reflection at 26°–28°, typical of crystalline graphitic layers of carbonaceous materials. The mean crystallite sizes of the primary the MOF-5 derivatives were calculated to be 17–35 nm by application of the Scherrer equation to the peak (1 0 1) (see Table 1).

An FE-SEM image of the synthesized MOF-5 (Fig. 2a) shows a well-defined cubic morphology typical of Zn-based isoreticular
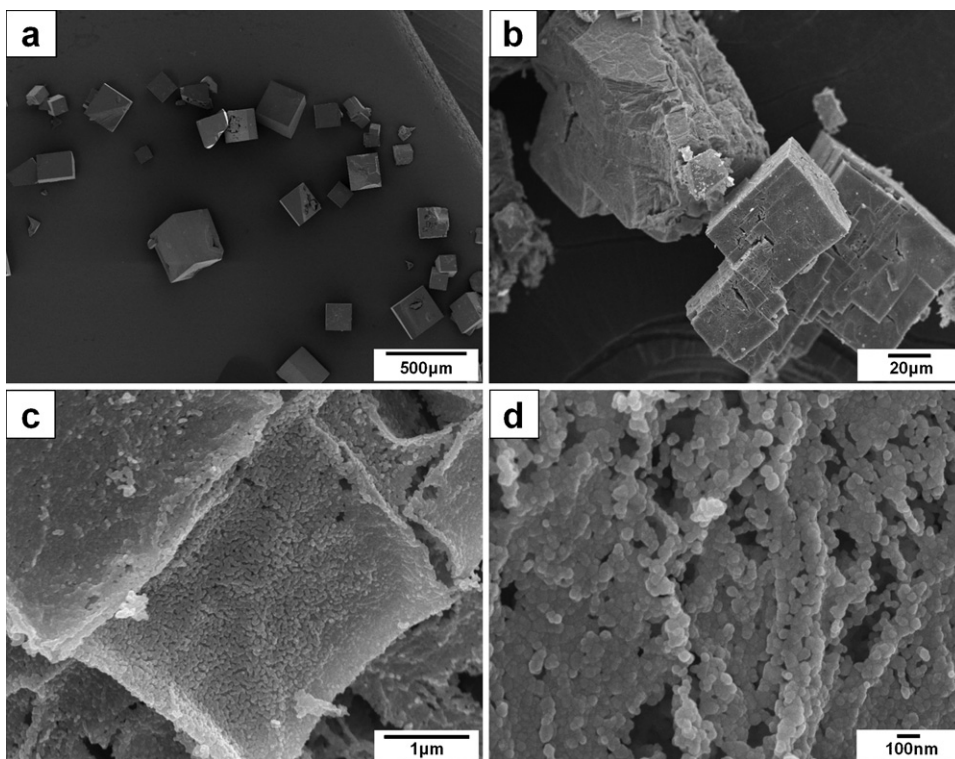
Fig. 2. FE-SEM images of (a) MOF–5, (b), (c), and (d) correspond to products prepared in air (sample code: 600A).

Table 1
Crystallite sizes obtained for the (1 0 1) diffraction peak.

Sample	600A	600A_3h	700A	600N	600N_3h
Crystal size (nm)	20.7	29.7	34.9	25.7	25.2

MOFs, indicating that the synthetic conditions were adequate for preparing MOF-5. Interestingly, the product of thermal decomposition of MOF-5 under air maintained the cubic morphology (Fig. 2b). Enlarged views (Fig. 2c and d) clearly indicated that the three-

dimensional (3D) cubic structure of MOF-5 was reorganized into aggregates of ZnO nanoparticles with a 3D cubic morphology. To the best of our knowledge, aggregates of ZnO nanoparticles with hierarchical 3D cubic architectures have not been reported previously.

Interestingly, the MOF-derivatives prepared under nitrogen gas retained their overall cubic structure (Fig. 3a). However, enlarged views displayed somewhat different morphological structures (Fig. 3b and c). In comparison with the samples prepared in air, the product obtained showed hexagonal faceted crystalline ZnO
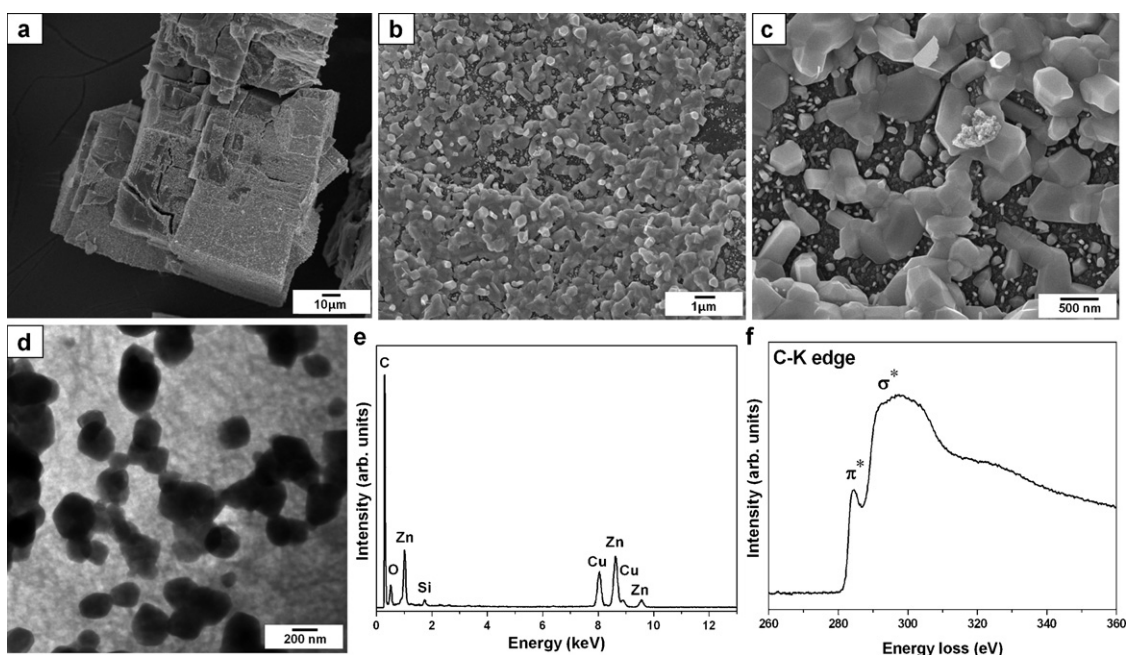

Fig. 3. (a), (b), and (c) FE-SEM images, (d) TEM image, (e) EDS spectrum, and (f) EEL spectrum of the obtained product prepared under nitrogen (sample code: 600N_3h).

clusters embedded in the carbonaceous matrix. The ZnO@C composite microstructure was further confirmed by TEM imaging and EDS analysis (Fig. 3d and e). The TEM image clearly showed the presence of transparent layers in the synthesis mixture, indicating thin carbonaceous layers with a low electron density (Fig. 3d). The transparency of the carbon substrate suggested that the obtained product had a high porosity. The ED spectrum (Fig. 3e) of the synthesized product validated the presence of carbon atoms. The copper and silicon peaks were attributed to the copper grid and silicon detector, respectively. The EEL spectrum of the sample showed a well-defined C-K edge characteristic of carbonaceous species in the range 280–300 eV (Fig. 3f). The EEL spectrum showed that the C-K edge was divided into two peaks, π^* (284 eV) and σ^* (291 eV) pre-ionizations, which indicated the presence of sp^2 and sp^3 bonding in the carbonaceous species [21,22].

The textural characteristics of the product were investigated by measuring the nitrogen adsorption isotherms, as shown in Fig. 4. The isotherms of the samples prepared under air (Fig. 4a) were type II isotherms with a sharp increase over the range 0.8–1.0 relative pressure, corresponding to non-porous or macroporous materials. These materials showed very low SSAs (7–12 m^2/g SSA, fit using the BET equation) and total pore volumes (0.02–0.05 cm^3/g), typical of ZnO (Table 2). In contrast, the samples prepared under nitrogen displayed significantly higher nitrogen uptake capacities (Fig. 4b). The shape of the nitrogen isotherms resembled a combined type I/IV isotherm: a steep increase at low relative pressure and the following small slope at intermediate relative pressure occurred concomitantly with the desorption hysteresis, revealing the presence of a combination of micropores (<2 nm) and mesopores (2–50 nm) in the samples [23]. From these isotherms, the calculated BET SSAs exceeded 500 m^2/g, and micro- and mesoporosity were present concurrently (Table 2).

3.2. Rhodamine B adsorption capacity of the products

Fig. 5 shows the RhB adsorption capacities of the samples prepared in air, P25, or ST01. Adsorption–desorption equilibrium was reached within 30 min for most samples, as reported previously [24,25]. It should be noted that the adsorption capacities of each sample were about the same, despite significant differences in SSA (ST01: 273 m^2/g and 600A: 12 m^2/g). The quantities associated with saturated adsorption on both commercial P25 and ST01 samples were very low, clearly suggesting a weaker affinity of TiO_2 toward RhB compared with that of ZnO [26]. The other samples obtained also adsorbed only small amounts of RhB, and all measured values were below 10%.

Adsorption values for samples prepared under nitrogen are shown in Fig. 6. The RhB dye was thoroughly decolorized within 30 min in the presence of the 600N sample. Moreover, the sample adsorbed RhB faster in the second cycle of the repeatability test
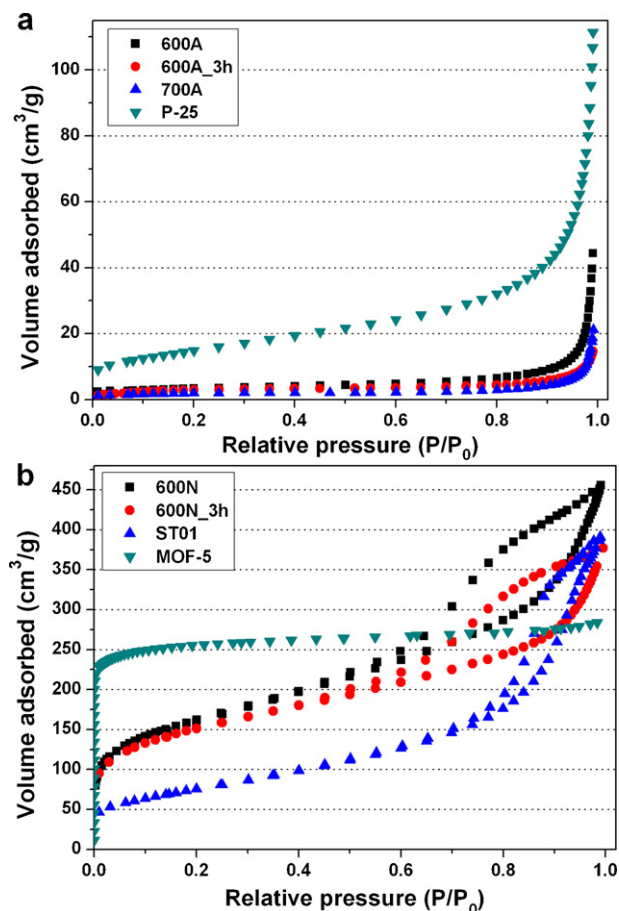

Fig. 4. Nitrogen adsorption isotherms at 77 K of (a) the products prepared in air, and (b) the products prepared under nitrogen.

than in the first cycle. This property was retained to the seventh cycle test, demonstrating that the porous carbonaceous layer in the sample adsorbed relatively enormous quantities of RhB (Fig. 6b). Furthermore, the adsorption capacity of the product synthesized under nitrogen was one of the highest among materials reported to have high adsorption capacities for organic dyes [24–26].

The adsorption capacities of the 600N and 600N_3h were more than 100 times greater than the capacity of ST01, whereas the SSA of the samples were higher than that of ST01 by only a factor of 2. The main driving force for dye adsorption by carbonaceous species was attributed to the π–π interactions between the graphitic carbon layer (sp^2 bonding) and the aromatic rings of the dye molecules [26]. The sp^2 character (see the EELS results shown in Fig. 2f) of the samples provides a rationale for the superior adsorption per-

Table 2
Pore characteristics determined from the nitrogen adsorption isotherms of the products at 77 K.

Sample	BET SSA[a] (m^2/g)	Langmuir SSA[b] (m^2/g)	t-Plot micropore volume (cm^3/g)	BJH adsorption cumulative volume (1.7 and 300 nm) (cm^3/g)	Total pore volume at 0.98 of relative pressure (cm^3/g)
MOF-5	1005	1109	0.337	0.09	0.44
600A	12	16	0	0.04	0.05
600A_3h	11	16	0	0.02	0.02
700A	7	10	0	0.02	0.02
600N	576	788	0.05	0.62	0.67
600N_3h	538	737	0.05	0.50	0.55
P25	53	75	0	0.12	0.13
ST01	273	377	0.01	0.59	0.59

[a] SSA, specific surface area, determined by the BET equation.
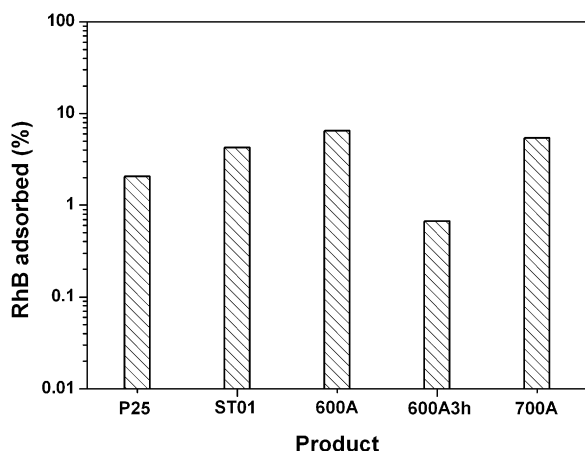[b] Determined by the Langmuir equation.

Fig. 5. RhB adsorption capacities of two commercial TiO$_2$ (P25 and ST01) and the products prepared in air.

Fig. 7. Pore size distribution of the products, analyzed using the BJH equation.

formance [21]. To further investigate the origin of the adsorption performance, we calculated the pore size distributions of the samples and ST01 using the BJH equation, as shown in Fig. 7. RhB molecules are about 1.5 nm in size, as estimated by a previous computer simulation study [27,28]. The optimal pore size for adsorption was previously determined to be 1.5–2 times larger than the size of the target molecule [29]. Thus, a pore size of 2–3 nm should be
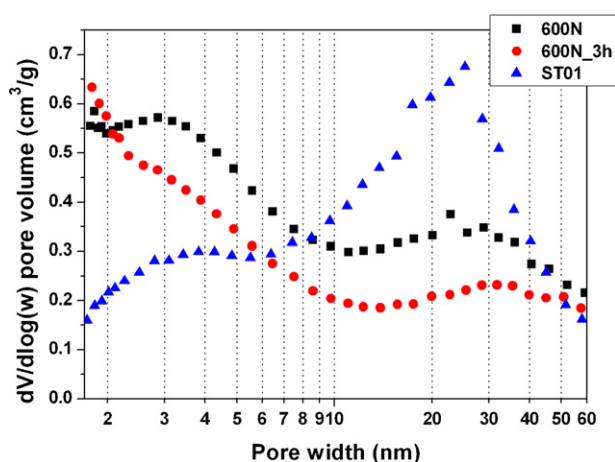
optimal for the effective adsorption of RhB. The pore size distribution suggested that the superior adsorption capacity stemmed from the high volume of pores of size 2–3 nm in the obtained samples. In contrast, the relatively large pore size of ST01 resulted in a poor adsorption capacity for organic dyes, despite the high SSA.
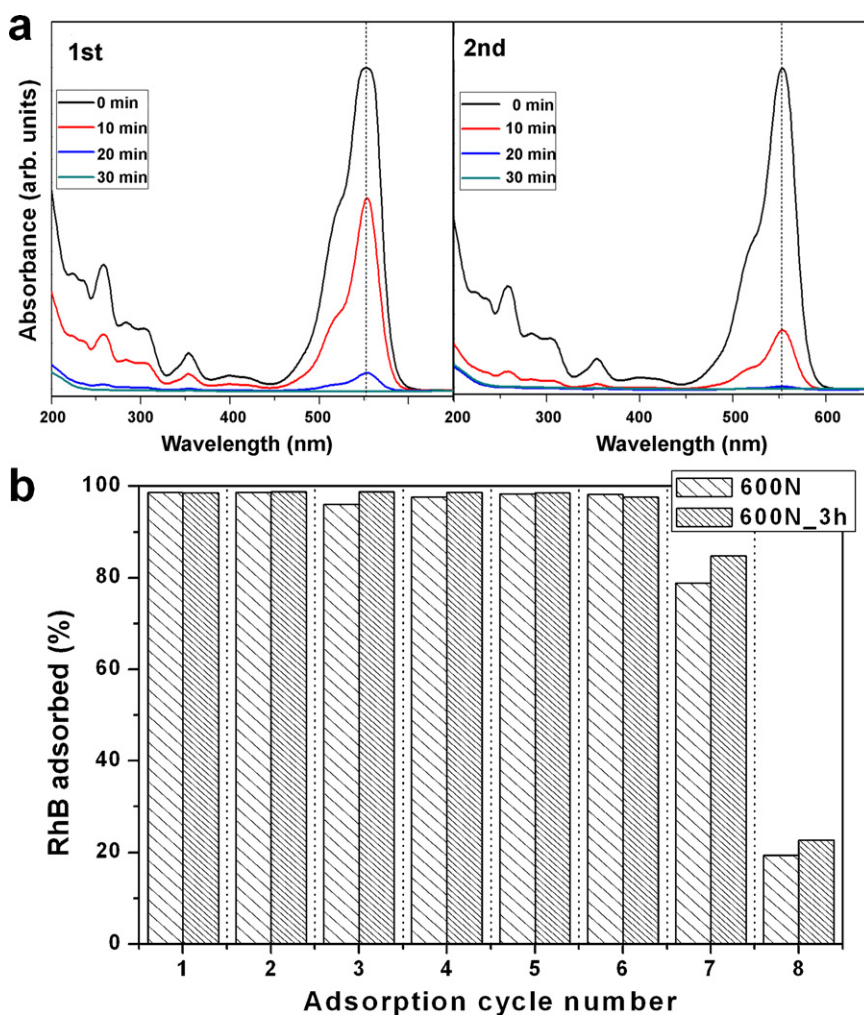

Fig. 6. (a) The RhB adsorption repeatability test based on the UV–vis spectral changes, and (b) total adsorption capacities of the products prepared under nitrogen.
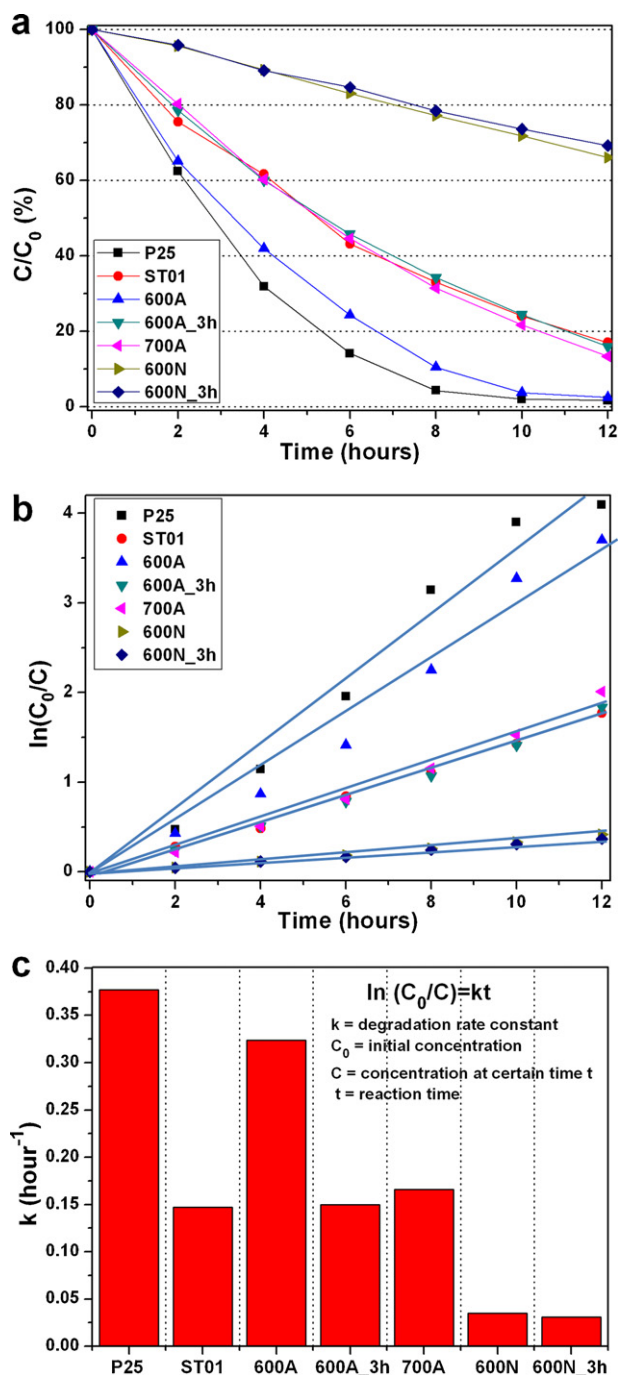
Fig. 9. PL spectra of the products prepared in air.

reduced photocatalytic activity in reported works [24]. Interestingly, 600A was found to have an activity comparable to that of P25 with an enhanced activity compared to ST01. Furthermore, 600A_3h and 700A showed slightly higher activities than ST01. The samples (600N and 600N_3h) prepared under nitrogen exhibited relatively low activity due to the large quantities of porous carbon present in the samples. The photodegradation data in Fig. 8a may be presented as logarithmic plots, as shown in Fig. 8b, because the photodegradation of RhB obeyed first-order kinetics [24,26,30]. Thus, the slope of the graphs in Fig. 8b provided quantitative estimates for the photocatalytic activity of the samples (Fig. 8c). The slope demonstrated that a selection of the obtained samples may provide ZnO-based photocatalysts for the elimination of organic pollutants from wastewater.

The outstanding photocatalytic activity of 600A was investigated by measuring the room temperature PL (excitation wavelength: 325 nm) of samples prepared in air (Fig. 9). All spectra revealed UV–green band emission originating from surface defect levels associated with oxygen vacancies or interstitial zinc [31,32]. Unlike the other samples, the PL spectrum of 600A was significantly quenched in the UV range 390–410 nm, indicating that the rate of recombination between the photogenerated holes and electrons was lowered on the surface of the prepared ZnO crystal [24,33,34]. Therefore, a lower recombination rate supported the superior photocatalytic activity of the 600A.

4. Conclusions

In conclusion, novel ZnO-based nanostructured architectures were successfully synthesized via simple heat treatment of MOF-5 under different atmospheric conditions. In air, MOF-5 was transformed into hierarchical aggregates of ZnO nanoparticles with 3D cubic morphologies. The resultant materials showed good photocatalytic activity with respect to RhB degradation, such that the degradation rate constants were comparable to that of commercial P25 and much higher than that of ST01. Contrasting with the ZnO nanoparticles, the ZnO@C hybrid composites were generated by heat treatment of MOF-5 under nitrogen. The hybrid composites possessed high porosity with pore sizes that were adequate for adsorbing RhB. The resulting adsorption capacities were superior compared with those of porous ST01. These results suggest that ZnO-based photocatalysts perform as well as commercial TiO₂ photocatalysts. This approach presents a new direction for MOF research and potential applications.

Fig. 8. (a) Photodegradation of RhB as a function of UV irradiation time in the presence of the prepared products. (b) Linear-log plot of (a). (c) Degradation rate constants of the products.

3.3. Photocatalytic decomposition activity of the products

The photocatalytic activities of the obtained products, commercial P25, and ST01, were evaluated by measuring the decomposition of RhB under UV irradiation. Fig. 8a shows the photocatalytic decomposition of RhB monitored according to the normalized residual concentration change versus time for the various samples. As seen in Fig. 8a, the commercial TiO₂ materials P25 and ST01 decomposed 98 and 83% of the RhB, respectively, after irradiation with UV light for 12 h. TiO₂ has previously been described as a good candidate photocatalyst compared with ZnO, which has shown
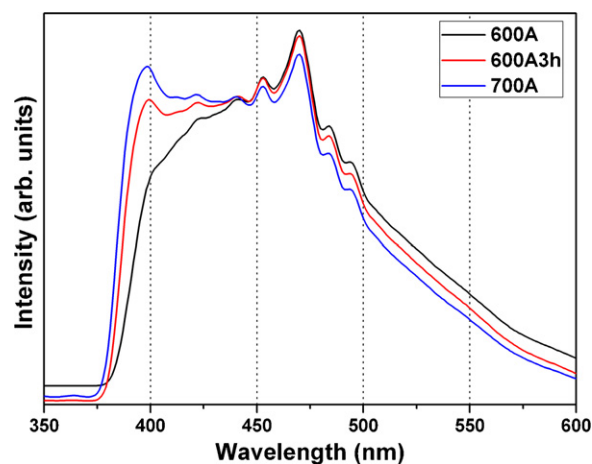
Acknowledgement

References

[1] H.K. Chae, D.Y. Siberio-Perez, J. Kim, Y. Go, M. Eddaoudi, A.J. Matzger, M. O'Keeffe, O.M. Yaghi, A route to high surface area, porosity and inclusion of large molecules in crystals, Nature 427 (2004) 523–527.

[2] J. Hafizovic, M. Bjorgen, U. Olsbye, P.D.C. Dietzel, S. Bordiga, C. Prestipino, C. Lamberti, K.P. Lillerud, The inconsistency in adsorption properties and powder XRD data of MOF-5 is rationalized by framework interpenetration and the presence of organic and inorganic species in the nanocavities, J. Am. Chem. Soc. 129 (2007) 3612–3620.

[3] H. Li, M. Eddaoudi, M. O'Keeffe, O.M. Yaghi, Design and synthesis of an exceptionally stable and highly porous metal-organic framework, Nature 402 (1999) 276–279.

[4] N.L. Rosi, J. Eckert, M. Eddaoudi, D.T. Vodak, J. Kim, M. O'Keeffe, O.M. Yaghi, Hydrogen storage in microporous metal-organic frameworks, Science 300 (2003) 1127–1129.

[5] J.L.C. Rowsell, A.R. Millward, K.S. Park, O.M. Yaghi, Hydrogen sorption in functionalized metal-organic frameworks, J. Am. Chem. Soc. 126 (2004) 5666–5667.

[6] S.J. Yang, J.Y. Choi, H.K. Chae, J.H. Cho, K.S. Nahm, C.R. Park, Preparation and enhanced hydrostability and hydrogen storage capacity of CNT@MOF-5 hybrid composite, Chem. Mater. 21 (2009) 1893–1897.

[7] B.L. Chen, C.D. Liang, J. Yang, D.S. Contreras, Y.L. Clancy, E.B. Lobkovsky, O.M. Yaghi, S. Dai, A microporous metal-organic framework for gas-chromatographic separation of alkanes, Angew. Chem. Int. Ed. 45 (2006) 1390–1393.

[8] S. Kitagawa, R. Kitaura, S. Noro, Functional porous coordination polymers, Angew. Chem. Int. Ed. 43 (2004) 2334–2375.

[9] A. Kuc, A. Enyashin, G. Seifert, Metal-organic frameworks: structural, energetic, electronic, and mechanical properties, J. Phys. Chem. B 111 (2007) 8179–8186.

[10] S. Bordiga, C. Lamberti, G. Ricchiardi, L. Regli, F. Bonino, A. Damin, K.P. Lillerud, M. Bjorgen, A. Zecchina, Electronic and vibrational properties of a MOF-5 metal-organic framework: ZnO quantum dot behaviour, Chem. Commun. (2004) 2300–2301.

[11] F.X.L.I. Xamena, A. Corma, H. Garcia, Applications for metal-organic frameworks (MOFs) as quantum dot semiconductors, J. Phys. Chem. C 111 (2007) 80–85.

[12] S.S. Kaye, A. Dailly, O.M. Yaghi, J.R. Long, Impact of preparation and handling on the hydrogen storage properties of Zn4O(1,4-benzenedicarboxylate)(3) (MOF-5), J. Am. Chem. Soc. 129 (2007) 14176–14177.

[13] X. Qin, L.Q. Jing, G.H. Tian, Y.C. Qu, Y.J. Feng, Enhanced photocatalytic activity for degrading Rhodamine B solution of commercial Degussa P25 TiO2 and its mechanisms, J. Hazard. Mater. 172 (2009) 1168–1174.

[14] N. Iwashita, C.R. Park, H. Fujimoto, M. Shiraishi, M. Inagaki, Specification for a standard procedure of X-ray diffraction measurements on carbon materials, Carbon 42 (2004) 701–714.

[15] A. Dailly, J.J. Vajo, C.C. Ahn, Saturation of hydrogen sorption in Zn benzenedicarboxylate and Zn naphthalenedicarboxylate, J. Phys. Chem. B 110 (2006) 1099–1101.

[16] L.M. Huang, H.T. Wang, J.X. Chen, Z.B. Wang, J.Y. Sun, D.Y. Zhao, Y.S. Yan, Synthesis, morphology control, and properties of porous metal-organic coordination polymers, Micropor. Mesopor. Mater. 58 (2003) 105–114.

[17] S.J. Yang, C.R. Park, Facile preparation of monodisperse ZnO quantum dots with high quality photoluminescence characteristics, Nanotechnology 19 (2008) 035609.

[18] A. Akyol, M. Bayramoglu, Photocatalytic performance of ZnO coated tubular reactor, J. Hazard. Mater. 180 (2010) 466–473.

[19] S. Anas, R.V. Mangalaraja, S. Ananthakumar, Studies on the evolution of ZnO morphologies in a thermohydrolysis technique and evaluation of their functional properties, J. Hazard. Mater. 175 (2010) 889–895.

[20] H. Thakuria, B.M. Borah, G. Das, ZnO nanoparticles from a metal-organic framework containing Zn-II metallacycles, Eur. J. Inorg. Chem. (2007) 524–529.

[21] S.J. Yang, J.H. Cho, G.H. Oh, K.S. Nahm, C.R. Park, Easy synthesis of highly nitrogen-enriched graphitic carbon with a high hydrogen storage capacity at room temperature, Carbon 47 (2009) 1585–1591.

[22] S. Urbonaite, S. Wachtmeister, C. Mirguet, E. Coronel, W.Y. Zou, S. Csillag, G. Svensson, EELS studies of carbide derived carbons, Carbon 45 (2007) 2047–2053.

[23] D.W. Wang, F. Li, M. Liu, G.Q. Lu, H.M. Cheng, 3D aperiodic hierarchical porous graphitic carbon material for high-rate electrochemical capacitive energy storage, Angew. Chem. Int. Ed. 47 (2008) 373–376.

[24] D.D. Lin, H. Wu, R. Zhang, W. Pan, Enhanced photocatalysis of electrospun Ag–ZnO heterostructured nanofibers, Chem. Mater. 21 (2009) 3479–3484.

[25] P.F. Ji, J.L. Zhang, F. Chen, M. Anpo, Study of adsorption and degradation of acid orange 7 on the surface of CeO2 under visible light irradiation, Appl. Catal. B-Environ. 85 (2009) 148–154.

[26] Y.C. Hsu, H.C. Lin, C.W. Lue, Y.T. Liao, C.M. Yang, A novel synthesis of carbon-coated anatase nanocrystals showing high adsorption capacity and photocatalytic activity, Appl. Catal. B-Environ. 89 (2009) 309–314.

[27] J.H. Huang, K.L. Huang, S.Q. Liu, A.T. Wang, C. Yan, Adsorption of Rhodamine B and methyl orange on a hypercrosslinked polymeric adsorbent in aqueous solution, Colloids Surf. A 330 (2008) 55–61.

[28] M. Asilturk, F. Sayilkan, S. Erdemoglu, M. Akarsu, H. Sayilkan, M. Erdemoglu, E. Arpac, Characterization of the hydrothermally synthesized nano-TiO2 crystallite and the photocatalytic degradation of Rhodamine B, J. Hazard. Mater. 129 (2006) 164–170.

[29] I. Cabria, M.J. Lopez, J.A. Alonso, The optimum average nanopore size for hydrogen storage in carbon nanoporous materials, Carbon 45 (2007) 2649–2658.

[30] W.Y. Dong, C.W. Lee, X.C. Lu, Y.J. Sun, W.M. Hua, G.S. Zhuang, S.C. Zhang, J.M. Chen, H.Q. Hou, D.Y. Zhao, Synchronous role of coupled adsorption and photocatalytic oxidation on ordered mesoporous anatase TiO2–SiO2 nanocomposites generating excellent degradation activity of RhB dye, Appl. Catal. B-Environ. 95 (2010) 197–207.

[31] B. Reeja-Jayan, E. De la Rosa, S. Sepulveda-Guzman, R.A. Rodriguez, M.J. Yacaman, Structural characterization and luminescence of porous single crystalline ZnO nanodisks with sponge-like morphology, J. Phys. Chem. C 112 (2008) 240–246.

[32] U. Pal, C.W. Kim, N.A. Jadhav, Y.S. Kang, Ultrasound-assisted synthesis of mesoporous ZnO nanostructures of different porosities, J. Phys. Chem. C 113 (2009) 14676–14680.

[33] J.H. Sun, S.Y. Dong, Y.K. Wang, S.P. Sun, Preparation and photocatalytic property of a novel dumbbell-shaped ZnO microcrystal photocatalyst, J. Hazard. Mater. 172 (2009) 1520–1526.

[34] L.Y. Yang, S.Y. Dong, J.H. Sun, J.L. Feng, Q.H. Wu, S.P. Sun, Microwave-assisted preparation, characterization and photocatalytic properties of a dumbbell-shaped ZnO photocatalyst, J. Hazard. Mater. 179 (2010) 438–443.